Massive multi-mission statistical study and analytical modeling of the Earth's magnetopause: 2 - Shape and location

G. Nguyen [1], N.Aunai [1], B.Michotte de Welle [1], A.Jeandet [1], B.Lavraud [2]and D.Fontaine [1]

[1]CNRS, Ecole polytechnique, Sorbonne Université, Univ Paris Sud, Observatoire de Paris, Institut Polytechnique de Paris, Université Paris-Saclay, PSL Research Univsersity, Laboratoire de Physique des Plasmas, Palaiseau, France
[2]Laboratoire d'astrophysique de Bordeaux, Univ. Bordeaux, CNRS, B18N, allée Geoffroy Saint-Hilaire, 33615 Pessac, France
[3]Institut de Recherche en Astrophysique et Planétologie, Université de Toulouse, CNRS, CNES, Toulouse, France

Key Points:

- We use a multi-mission catalogs to provide a statistical analysis of the magnetopause location and shape.
- We confirm the expected influence of the solar wind dynamic pressure, of the IMF B_z component, of the Earth dipole tilt angle as well as the north-south asymmetry it induces.
- Varying IMF clock angle affects the level of flaring, resulting in an elliptic cross section in the cGSM YZ plane which major axis is oriented along the cGSM Y axis when the IMF is southward and along the cGSM X axis when the IMF is northward.

Corresponding author: Gautier Nguyen, gautier-mahe.nguyen@intradef.gouv.fr

Abstract

The Earth magnetopause is the boundary between the magnetosphere and the shocked solar wind. Its location and shape are primarily determined by the properties of the solar wind and interplanetary magnetic field (IMF) but the nature of the control parameters and to what extent they impact the stand-off distance, the flaring, and the symmetries, on the dayside and night side, is still not well known. We present a large statistical study of the magnetopause location and shape based an extensive multi-mission magnetopause database, cumulating 17 230 crossings on 17 different spacecraft, from the dayside to lunar nightside distances. The results confirm the power-law dependency of the stand-off position on the solar wind pressure. The IMF clock angle itself (all amplitudes combined) does not impact the stand-off distance, nor does the cone angle. However, the magnetopause is found to move Earthward as the IMF gets stronger and more southward. All upstream conditions combined, it is found that the function used at the root of several analytical models still holds at lunar distances. We find that the equatorial flaring is larger than the meridional one. However, the meridional flaring is found to depend on the seasonal tilt conditions, being larger in the summer hemisphere. The flaring is also found to depend on the IMF clock angle. Meridional flaring increases as the IMF turns south and is then larger than the equatorial flaring. The equatorial flaring barely changes or weakly increases as the IMF turns northward, and is larger than the meridional flaring for northward conditions. The results of the study pave the way for the elaboration of a new analytical empirical expression of the magnetopause location and shape.

1 Introduction

The Earth's magnetopause results from the interaction between the solar wind and the Earth magnetic field. Roughly located where the solar wind dynamic pressure and the Earth magnetic pressure balance, this current sheet marks the boundary of the Earth environment, confined from the solar wind by the frozen-in condition.

The first observation of the Earth magnetopause (Cahill & Amazeen, 1963), was followed by many observational and numerical studies that exhibited a strong influence of the different solar wind physical parameters on the magnetopause location and shape (Hasegawa (2012); Němeček et al. (2020) and references therein). Its first empirical and analytical modeling from Fairfield (1971) and Formisano (1979), based on the aforementioned pressure balance condition, has been done using IMP observations and a quadric surface shape.

From then on, several analytical empirical models parametrized by the solar wind dynamic pressure and the IMF B_z component were developed (Roelof & Sibeck, 1993; Petrinec & Russell, 1993). These models, that continued relying on the form of a quadric surface, were fitted using ISEE magnetopause crossings and progressively considered the extension of the magnetopause in the nightside (Petrinec & Russell, 1996). With the measurements of the IMP8, ISEE 1 and ISEE 2 spacecraft used simultaneously, Shue et al. (1997) improved the accuracy of the magnetopause models by considering an inverse trigonometric function still in use in the most recent models:

$$r = r_0 \left(\frac{2}{1 + \cos(\theta)} \right)^{\alpha} \tag{1}$$

where θ is the zenith angle defined in the Appendix A, r_0 is the radial distance of the magnetopause nose and α describes the flaring of the magnetopause along the GSM X axis.

All of the previously mentioned models used data from spacecraft that had an equatorial orbit and thus supposed a symmetry around the X axis. This symmetry was questioned by the investigation of Sotirelis and Meng (1999) that evidenced an influence of the Earth dipole tilt angle in accordance with the findings of Tsyganenko (1998). The influence of the

dipole tilt angle was later confirmed by Boardsen et al. (2000) and Eastman et al. (2000) using the Hawkeye measurements, and by the analysis of Interball data by Šafránková et al. (2002). Their observations also suggested an indentation of the magnetopause in the near-cusp region.

Using measurements of LANL and GOES, Kuznetsov and Suvorova (1998) evidenced the presence of a dawn-dusk asymmetry later also suggested by Dmitriev and Suvorova (1999) using an Artificial Neural Network on geosynchronous crossings. This asymmetry was later found to be linked to the aberration of the solar wind due to Earth orbital motion by Šafránková et al. (2002).

In the light of these new findings, Lin et al. (2010) proposed a new analytical magnetopause surface model fitted to the data, that took into consideration an azimuthal asymmetry induced by the dipole tilt angle and also kept the possibility of a dawn-dusk asymmetry despite of the correction brought to the data in order to remove the aberration.

Going further, Dušík et al. (2010) and Grygorov et al. (2017) used THEMIS data and pointed out that an increasing IMF B_x pulled the magnetopause sunward while the MHD simulations of Liu et al. (2015) indicated this component would rather also contribute to the north-south asymmetry already induced by the dipole tilt angle.

Their simulations also suggested that, for high mach numbers, increasing the IMF B_y component lead to a major axis of the magnetopause elliptic cross-section that follows the IMF orientation. This finding was also suggested at low Mach numbers by the simulations performed by (Lavraud & Borovsky, 2008; Lavraud et al., 2013) and were linked to the magnetic stress on the magnetopause that contracts it in a direction perpendicular to the IMF.

Despite this important number of studies, there are still numerous open questions:

1. First of all, the influence of the IMF cone angle is still unclear and the different conclusions drawn by Dušík et al. (2010) and Liu et al. (2015), that we just presented, call for further investigation.
2. Second, the influence of the IMF clock angle on the flaring has been suggested numerically by Liu et al. (2015) and Lavraud and Borovsky (2008). Yet, this influence still lacks of observational evidences and has not yet been considered by any empirical analytical model beyond the dependency on B_z.
3. Third, all of the magnetopause surface models considered data in the range $X > -40$ Re and are thus extrapolated to the far nightside whereas now spacecraft at lunar orbit such as ARTEMIS provide useful information on the shape of the magnetopause at these distances.
4. Fourth, different observations of the polar cusps crossings led to different conclusions regarding the shape of the magnetopause in this region. If Boardsen et al. (2000); Šafránková et al. (2002); Šafránková et al. (2005) suggested the existence of an indentation, Zhou and Russell (1997); Lavraud, Fedorov, et al. (2004) suggested the opposite. Eastman et al. (2000) inferred that these divergences could be explained by the definition of the magnetopause considered by each study. Using Cluster data polar cusp events, Lavraud, Phan, et al. (2004) suggested that the indentation was observed because the inner cusp boundary was considered instead of the external one associated with the kinked field lines convected tailward or sunward depending on the IMF Bz, and for which the authors noticed no specific depletion. Consequently, the question of the shape of the magnetopause in the high-altitude near-cusp region is still open and requires additional investigations.

In this paper, we exploit the multi-mission the magnetopause crossings catalog elaborated with the gradient boosting developed in Nguyen et al. (2020a), one of the three companion papers of this study, to address the three first points mentioned above through a

statistical study of the location and shape of the magnetopause as a function of the different solar wind and IMF parameters. The results presented here will then lead to the construction of a new analytical and dynamical model of the magnetopause surface as a function of relevant upstream and seasonal control parameters in the second companion paper of this study (hereafter Nguyen et al. (2020b)). The question of the indentation of the near-cusp magnetopause will then be addressed in the last companion paper of this study (hereafter Nguyen et al. (2020c)).

This paper is organized as follows: Section 2 presents the dataset of magnetopause crossings we use and the associated upstream solar wind and IMF conditions, Section 3 focuses on the evolution of the magnetopause nose, Section 4 evidences the different magnetopause asymmetries and Section 5 investigates the different solar wind parameters that influence the flaring level of the magnetopause.

2 Dataset

The detection of 15 062 complete magnetopause crossings made by Nguyen et al. (2020a) offers an opportunity to provide a statistical insight on various geometrical properties of the magnetopause as functions of the upstream solar wind conditions. The 1 hour crossings constructed there are here reduced to 10 minutes crossings centered around the beginning of the ending time[1] of the largest magnetosheath interval detected by the region classifier. Each crossing is then associated to a set of solar wind upstream conditions obtained with a temporal shift of OMNI data. We determine this shift time by applying the two-step propagation algorithm presented in Šafránková et al. (2002). Using this method, we removed 772 crossings that had no available upstream solar wind condition.

We increase our dataset through the addition of the 2168 online[2] crossings of the missions IMP, ISEE, Geotail, Prognoz, Hawkeye, AMPTE, Explorer and OGO for which $X > -70$ Re, the farthest distance for which we detected ARTEMIS crossings. that were used in the comparison of Liu et al. (2015)'s model to observational data. The Hawkeye crossings were also used by Lin et al. (2010), especially when looking at the near-cusp magnetopause.

The combination of the two lists results in an ensemble of 17230 magnetopause crossings distributed on 17 different spacecraft. Contrary to the dataset presented by Wang et al. (2013), which has a similar number of crossings, the automated subset of our dataset does not consider any partial crossing, for which upstream solar wind conditions are likely to be the same. We thus expect our dataset to offer a wider range of solar wind and seasonal conditions at all altitudes and longitudes.

The summary of all the crossings in use in the present study and the mission they are associated with are shown in the Table 1.

Having merged the two lists, we correct the GSM position of each of the obtained 17230 magnetopause crossings by removing the aberration due to the Earth's revolution using a similar approach as Lin et al. (2010) and Boardsen et al. (2000), assuming a revolution velocity of 30 km/s. In the following, the positions we consider will then be expressed in the so-called cGSM coordinate system.

The histograms of the solar wind parameters associated to the crossings are shown with the blue bins in Figure 1 and compared to the histograms of the OMNI physical parameters measured between 2001 and 2019, shown with the red bins on the same Figure. For each panel, the two distributions are similar. This indicates that the greatest part of the crossings

[1] depending on whether the crossing is unbound or outbound

[2] `ftp://nssdcftp.gsfc.nasa.gov/spacecraftdata/magnetopausecrossings`

Mission	Number of Crossings	Mission	Number of Crossings
IMP	75	ISEE	333
Geotail	76	Prognoz	91
Hawkeye	1484	AMPTE	60
Explorer	17	OGO	32
THEMIS*	9311	Double Star*	891
MMS*	805	Cluster*	3353
ARTEMIS*	702	**Total**	17230

Table 1. Summary of the 17230 events that constitute our dataset. The missions denoted with an asterisk indicate the missions for which the magnetopause crossings have been obtained using the region classifier developed in Nguyen et al. (2020a).

occurred under normal solar wind conditions and these are the conditions under which we expect the statistics presented in this paper to be the most relevant.

As half of our crossings have been measured by spacecraft with relatively low apogees ($\sim$ 12 R_e), it is important to make sure that our dataset is free from any orbital bias. Such limitations could indeed affect the importance of the different dependencies we will be focusing on in the next sections as discussed in Němeček et al. (2020).

To do so, we show in Figure 2 the projections in the $(X-Y)$ and the $(X-Z)$ plane of the crossings corrected position. The grey shading represents the time during which the different spacecraft were at given coordinates (X, Y) and (X, Z). In both cases and for each value of X, the crossing with the highest Y or Z is located far from the maximal Y or Z reached by the spacecraft during the orbit. This suggests the crossings we selected are not limited by the orbit of the spacecraft we consider in this study.

This is also confirmed by Figure 3 that represents the histograms of the solar wind parameters for both the entire dataset and the crossings measured by the spacecraft that have a high apogee (above 12 Re). Having similar blue and red histograms for each panel ensures no orbital bias is introduced whatever solar wind parameter is considered.

The crossings are evenly distributed in the $(X-Y)$ plane however most of them are made at high-latitude in the northern hemisphere. We balance this distribution by adding for each crossing, its symmetric with opposite Z coordinate and tilt angle γ, in a similar way as done in Wang et al. (2013), assuming de facto that the northern summer hemisphere of the magnetopause is the symmetric the southern winter hemisphere: $r(X,Y,Z,\gamma) = r(X,Y,-Z,-\gamma)$.

In addition to the cGSM (X,Y,Z) cartesian coordinates, we will also use the spherical coordinates (R,θ,ϕ) defined following the convention presented in the Appendix A.

As mentioned in the introduction, the actual shape of the near-cusp magnetopause is still an open question and constitutes the main topic of Nguyen et al. (2020c) that comes as a companion paper of this study. In this study, we restrict our dataset to the 29077 crossing that are expected to occur outside of the cusp region. Following the indentation expression detailed by Lin et al. (2010), we define those so-called "out of cusp" crossings as the events for which the spherical coordinates θ and ϕ verify:

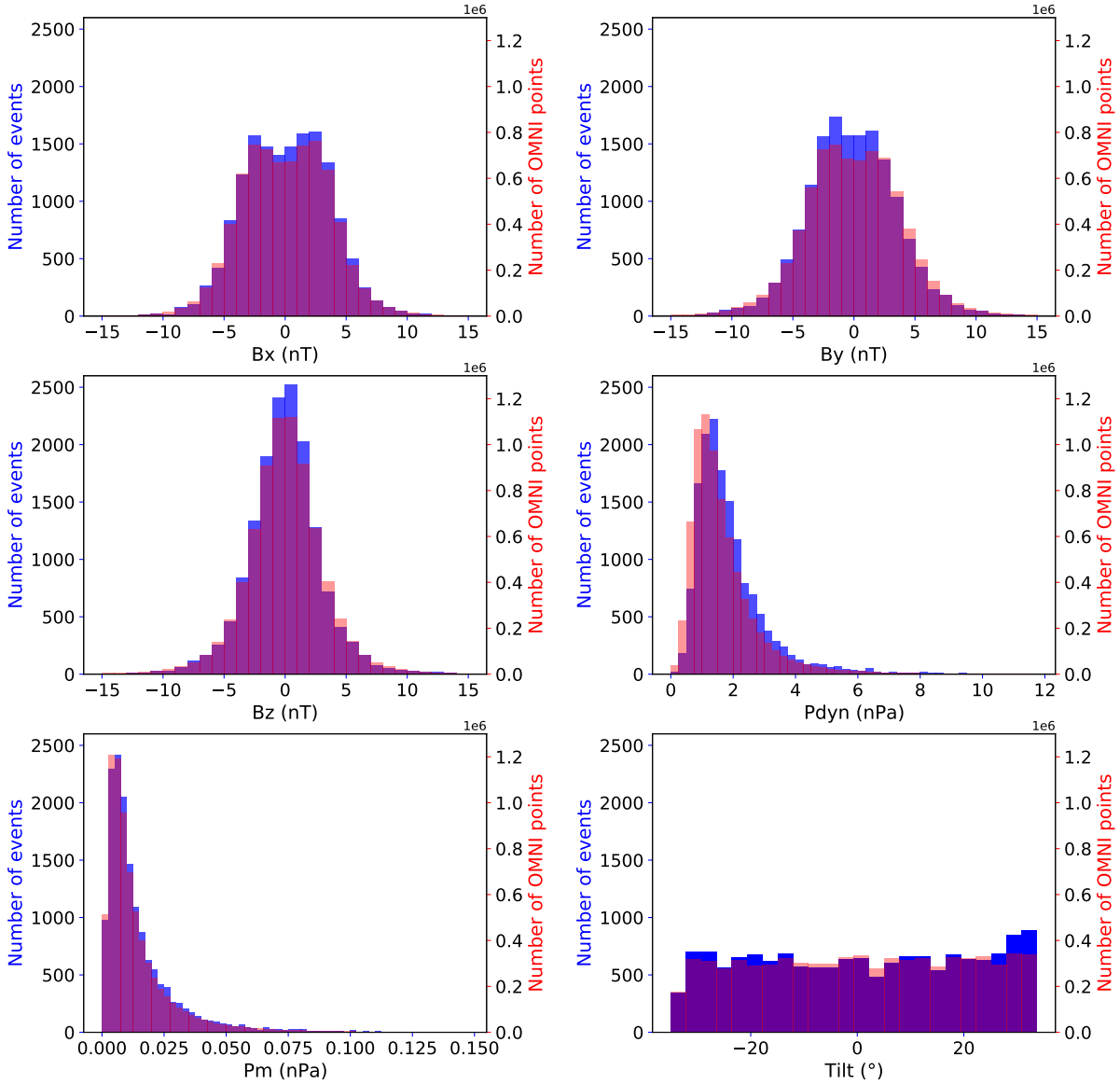

Figure 1. Statistical distribution of the solar wind parameters of the 17230 magnetopause crossings: the three magnetic field components, B_x (*top left*), B_y (*top right*), B_z (*middle left*), the dynamic pressure P_{dyn} (*middle right*), the magnetic pressure P_m (*bottom left*) and the dipole tilt angle (*bottom right*). The red bins indicate the counterpart distribution of the physical parameters of OMNI data between 2001 and 2019

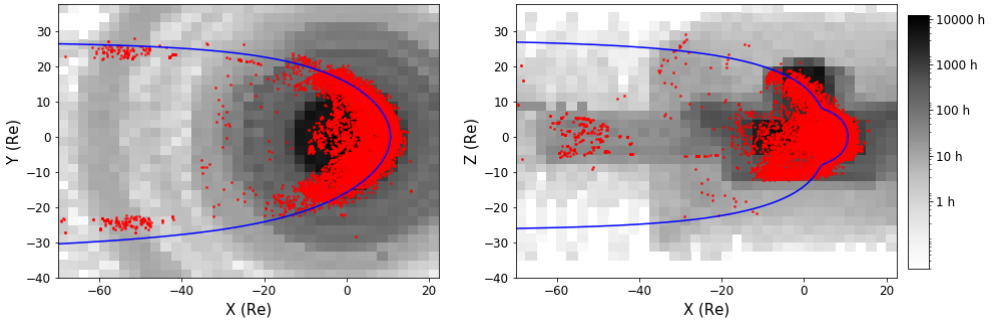

Figure 2. Projection in the $(X-Y)$ (*left*) and in the $(X-Z)$ (*right*) cGSM plane of the 17230 magnetopause crossings (red dots) The gray shading represents the time spent by all of the spacecraft in a given region of the $(X-Y)$ (resp. $(X-Z)$) plane. The blue line represent Lin et al. (2010) magnetopause model with a dynamic pressure of 2 nPa and a null Bz.

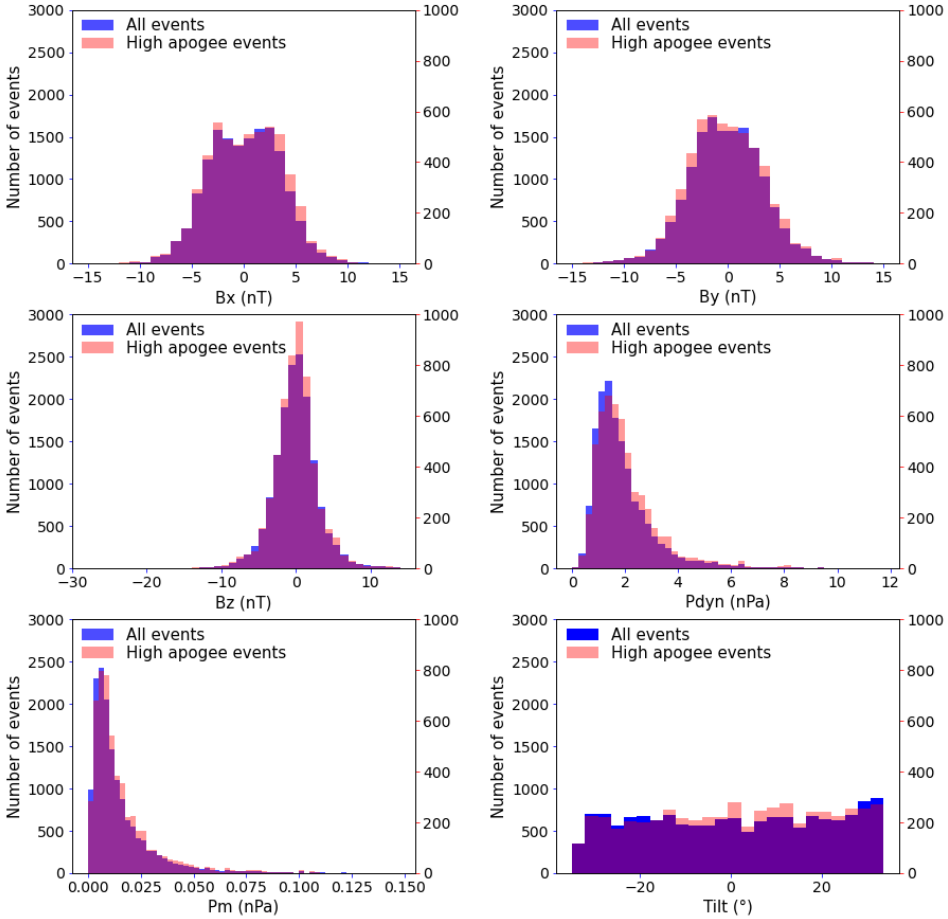

Figure 3. Histogram of the solar wind parameters of the 17230 magnetopause crossings. Each panel is the same than in Figure 1. The red here bins show the same distribution for the events measured by high apogee spacecraft

$$\begin{cases} (\theta-\theta_n)^2+\phi^2 \geq \left(-\frac{1}{d_n}\right)^{\frac{2}{a_{21}}} & \text{if } Z \geq 0 \\ (\theta-\theta_s)^2+\phi^2 \geq \left(-\frac{1}{d_s}\right)^{\frac{2}{a_{21}}} & \text{if } Z \leq 0 \end{cases} \tag{2}$$

$d_{n,s} = a_{16} \pm a_{17}\gamma + a_{18}\gamma^2$, $\theta_{n,s} = a_{19} \pm a_{20}\gamma$, and a_{21} represent the scope, the zenithal position and the shape of the polar cusps, γ is the Earth dipole tilt angle and $a_{16} = 2.60, a_{17} = 0.832, a_{18} = -5.328, a_{19} = 1.103, a_{20} = -0.907$ and $a_{21} = 1.450$ are the corresponding coefficients fitted by Lin et al. (2010). The crossings that are found inside of this so-defined cusp-indentation will constitute the core of the dataset used in Nguyen et al. (2020c).

3 The magnetopause subsolar stand-off distance

We study the magnetopause subsolar stand-off distance by selecting the 300 events for which $\theta < 7.50°$ and $Z > 0$ and approximate the magnetopause stand-off distance r_0 of these crossings by their actual radial distance r.

Naturally, we expect the total pressure $P_{dyn} + P_m$ to be the feature that has the greatest influence on the subsolar stand-off distance. Figure 4 represents the radial distance of the subsolar events subset as a function of the total pressure. The stand-off distance r_0 here appears to have a clear and consistent power-law dependency on the total pressure. This was already exhibited in observations by Shue et al. (1997) and numerically by Liu et al. (2015). We exhibit this dependency by fitting r_0 to the power law $a_0(P_{dyn}+P_m)^{a_1}$. The result of this fit is represented by the solid blue line and the grey interval that represents the 1-sigma confidence interval. The obtained values of a_0 and a_1 are shown in the top right corner of the Figure. a_0 represents the stand-off distance at 1 nPa and the obtained value is thus consistent with the typical value we expect for the subsolar magnetopause. We also find an exponent value of -0.161 for a_1, which is very close to the theoretical $-\frac{1}{6}$ and close to the values obtained by Shue et al. (1997), Lin et al. (2010) and Liu et al. (2015).

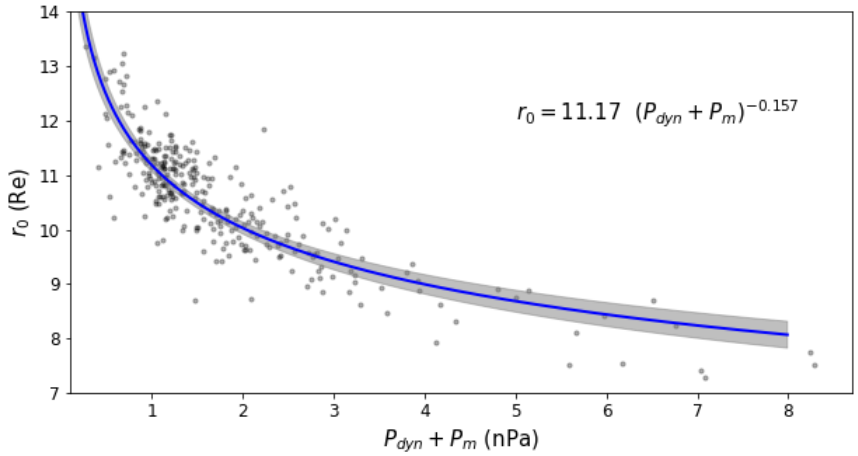

Figure 4. Variations of r_0 with the dynamic pressure. The solid blue line represent the fit of r_0 as a power-law of $P_{dyn} + P_m$ and the grey interval is the 1-sigma confidence interval of such fit.

The dependency on the solar wind ram and magnetic pressure is so strong that studying now the dependency of the standoff distance on the IMF orientation must be done with care.

To cope with it, we separate the 300 events into 30° wide bins of IMF cone (resp. clock) and fit r_0 as a power law of $(P_{dyn} + P_m)$ for each bin. We limit the bins for each angle by looking at the total number of each event per defined bin. This still offers a wide range of upstream IMF conditions of the same order as the ones used in the studies led by Roelof and Sibeck (1993) and Petrinec and Russell (1993).

We represent the evolution of the fitted stand-off distance at 1 nPa, the so-defined a_0, as a function of the IMF cone and clock angles with the black circles in the two panels of Figure 5.

Concerning the influence of the cone angle, first, we notice a small increase of a_0 as the IMF becomes more radial. This evolution is consistent with the findings of Dušík et al. (2010) or Grygorov et al. (2017) but in our case the effect an order of magnitude fainter. Their larger motion may be coming from their much broader angular selection, which may confuse flaring effects with the stand-off distance evolution. In both our case or theirs, the sunward motion is in the error bars of analytical models in that region and call for more future more detailed investigations. For now, as this influence appears to be negligible compared to the one of the total pressure, we will not consider it in the rest of the study.

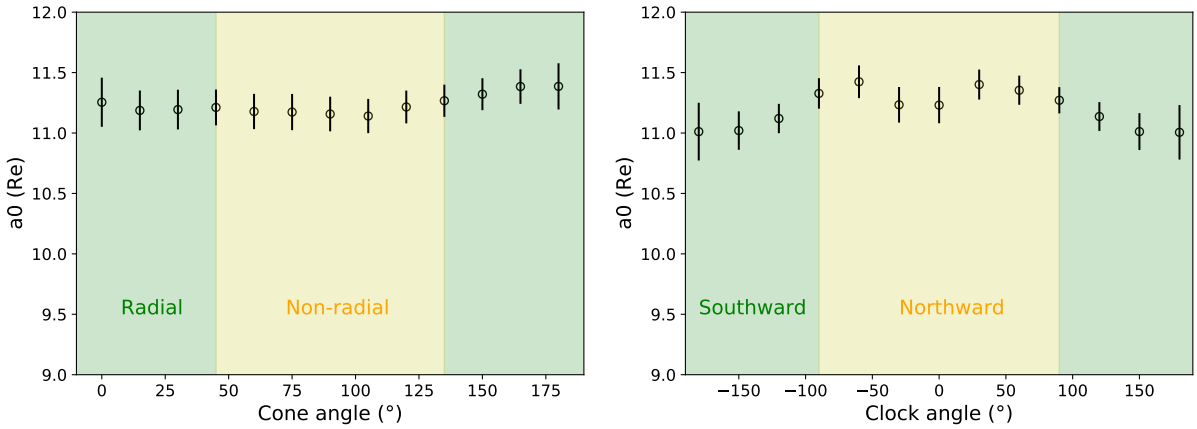

Figure 5. Evolution of the stand-off distance at 1 nPa, a_0 as a function of the IMF cone (*left*) and clock (*right*) angles. The black circles represent the value we obtain from fitting a power law to r_0 for different cone (resp. clock) angle bins. The error bars represent the 1-sigma confidence interval of such fits.

Concerning now the clock angle, the fits suggest an earthward motion of the magnetopause when the IMF turns from a northward to a southward orientation. Such motion is consistent with the picture of a subsolar magnetopause eroded by magnetic reconnection under a southward IMF. The motion could also be the consequence of a stronger Earthward magnetic force due to the enhanced magnetopause current in southward IMF. Whatever its cause, this motion barely stands out of the error bars and appears negligible compared to the one induced by the solar wind pressure to really consider the IMF clock angle actually has an influence on the magnetopause subsolar stand-off distance.

The clock angle does apparently not change a_0. However, it acts as a switch. Combined with an increasing IMF amplitude the clock orientation of the IMF can now indeed change a_0 significantly, as shown in the evolution of a_0 as a function of B_z on Figure 6. Here, the noticed decrease of a_0 for negative B_z is also consistent with the explanations given above. Those arguments may also explain the saturation of a_0 for positive B_z since magnetic

reconnection is not thought to occur and the magnetic shear is expected to be low at low latitude for a northward IMF.

For comparative purposes, the three colored dashed lines represent the evolution of a_0 with B_z previously obtained by Shue et al. (1997) (green line and equation 11 of the aforementioned paper), Lin et al. (2010) (red line and equation 20 of the aforementioned paper) and Liu et al. (2015) (blue line and equation 4 of the aforementioned paper). For northward IMF, the values of a_0 is consistent with the one obtained by both Shue et al. (1997) and Liu et al. (2015) while Lin et al. (2010)'s model over-estimates the stand-off distance by 2 Re. The three models also predict an earthward motion of the magnetopause for southward IMF and the slope of the decrease of a_0 for negative B_z is close from the one exhibited by Shue et al. (1997).

The studies of Liu et al. (2015) and Shue et al. (1997) suggest a saturation of a_0 for strong negative B_z (not shown in Figure 6) that confirms the observations made by Yang et al. (2002). In our case, even if the decrease of our fitted values of a_0 for negative B_z appears to be less important below -7 nT, the large error bars for this point and the restricted range of B_z values, due to the restriction of our dataset to the subsolar magnetopause, do not permit to draw any conclusion on what happens for extreme values of B_z. Subsolar magnetopause crossings under extreme B_z are extremely scarce and it is then of no use to study them from a statistical point of view for now. They however constitute excellent samples for further case studies on the behavior of the magnetosphere under extreme conditions, such as Interplanetary Coronal Mass Ejections.

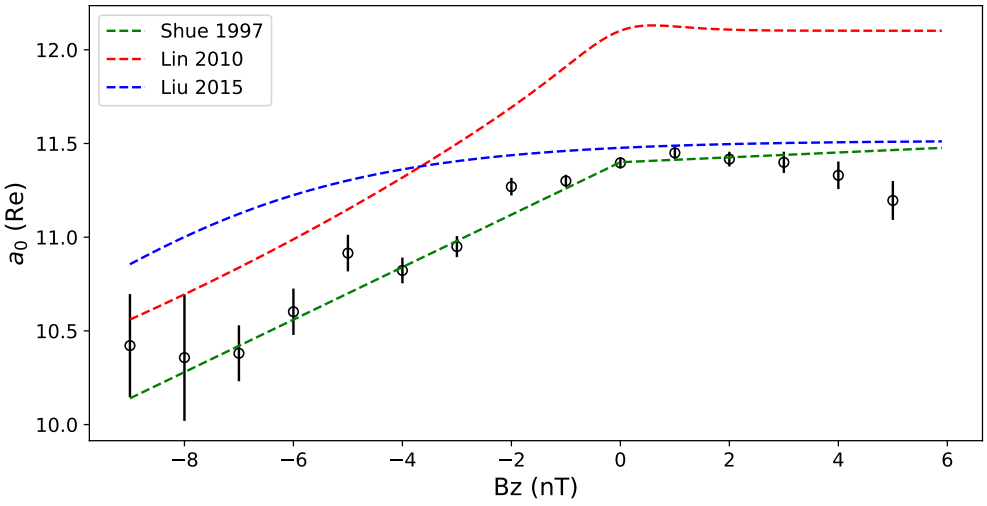

Figure 6. The same than Figure 5 but as a function of the IMF B_z. The three colored dashed line represent the evolution of a_0 according three previous existing models: Shue et al. (1997) (*green*), Lin et al. (2010) (*red*) and Liu et al. (2015) (*blue*).

We can use the two evolutions we exhibited to establish a primary empirical expression of the magnetopause stand-off distance in the form:

$$r_0 = \alpha_0 \left(1 + alpha_2 \tanh\left(\alpha_3 B_z + \alpha_4\right)\right) \left(P_{dyn} + P_m\right)^{-\alpha_1} \tag{3}$$

Applying the Levenberg-Marquardt algorithm (Newville et al., 2014) to our 300 subsolar crossings, we determine the values of the 5 α_i and then obtain:

$$r_0 = 10.91\,(1 + 0.039\tanh\,(0.65B_z + 2.0))\,(P_{dyn} + P_m)^{-0.153} \quad (4)$$

4 Asymmetries

The first empirical models (Fairfield, 1971; Formisano, 1979; Petrinec & Russell, 1993; Shue et al., 1997) of the magnetopause shape and location assumed axisymmetry around the cGSM X axis. Nevertheless, the MHD simulations of Lu et al. (2011) evidenced an asymmetry between the magnetopause flaring in the $(X-Y)$ plane and the flaring in the $(X-Z)$ plane. They evidenced the IMF B_z component and the Earth dipole tilt angle as the main actors at the origin of such azimuthal asymmetry. This asymmetry was considered by the models of Wang et al. (2013) and Lin et al. (2010) and already observed (Šafránková et al., 2002) but never confirmed in the far nightside, below -20 Re.

We address this question by selecting on one hand the 2047 events for which $|Y| < 2$ Re (the so-called $X-Z$ plane events) and on the other hand the 5443 events for which $|Z| < 1$ Re (the so-called $X-Y$ plane events). In both cases, we represent $\log(r)$, the radial distance of each crossing as a function of $\log\left(\frac{2}{1+\cos(\theta)}\right)$, the inverse trigonometric function especially considered by the models of Shue et al. (1997) and Liu et al. (2015), in the two panels of Figure 7. In both cases, we notice a linear dependency that legitimates this analytic expression. It is also worth noting that the linear dependency holds for the far nightside crossings of ARTEMIS giving in the process credit to using such an analytical expression.

The slope of a fitted linear expression should give a first estimate of the flaring coefficient α in both the $(X-Z)$ and the $(X-Y)$ planes. The red curve and the associated grey shading confidence intervals are shown in the two panels of Figure 7. We find a value of α that is lower in the $(X-Z)$ plane than in the $(X-Y)$ plane. Even if we lack observational evidences for the magnetopause at high latitude in the far nightside, this suggests the existence of an azimuthal asymmetry and a magnetopause that is more elongated in the Y-direction than in the Z-direction.

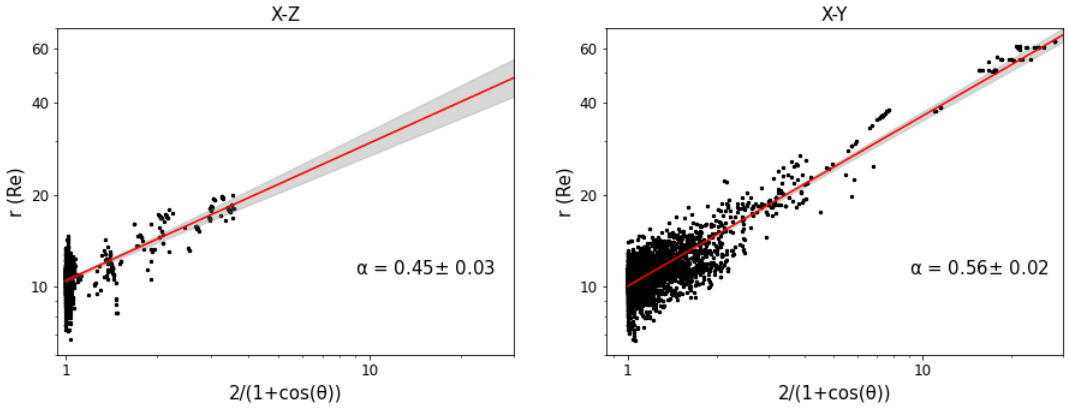

Figure 7. Evolution of the radial distance r of the crossings in the $(X-Z)$ (*left*) plane and in the $(X-Y)$ plane as a function of the inverted trigonometric function $\frac{2}{1+\cos(\theta)}$ on a logarithmic scale. The solid red line represent the linear fit of $\log r$ as a function of $\frac{2}{1+\cos(\theta)}$. The grey intervals represent the confidence intervals of such fits.

In addition to the azimuthal asymmetry, the MHD simulations of Liu et al. (2012) showed the dipole tilt angle induced a North-South asymmetry that was also observed by Boardsen et al. (2000) and considered by the fits of Lin et al. (2010) and Wang et al. (2013).

The symmetrization of the dataset that was done in section 2 allows this asymmetry and the evolution of the northern (or the southern) magnetopause flaring with the dipole tilt angle will be evidenced and investigated in the next subsection.

Following what we did to evidence the azimuthal asymmetry, we now separate the 5170 crossings located in the so-defined $(X-Y)$ plane into 3028 dawnward ($Y<0$) and 2415 duskward ($Y>0$) events and apply the same method as previously. The logarithm of the radial distance r of these two subsets of events as a function of the logarithm of the inverted trigonometric function $\frac{2}{1+\cos(\theta)}$ is shown in the Figure 8.

In this case, we obtain almost equal values for α on both sides, indicating no apparent dawn-dusk asymmetry and thus, a symmetric magnetopause regarding the $Y=0$ plane. In the light of those results, we decide to add another symmetry to the dataset by reverting the Y coordinate, increasing the size of the out of cusps crossings from 31671 to 63344.

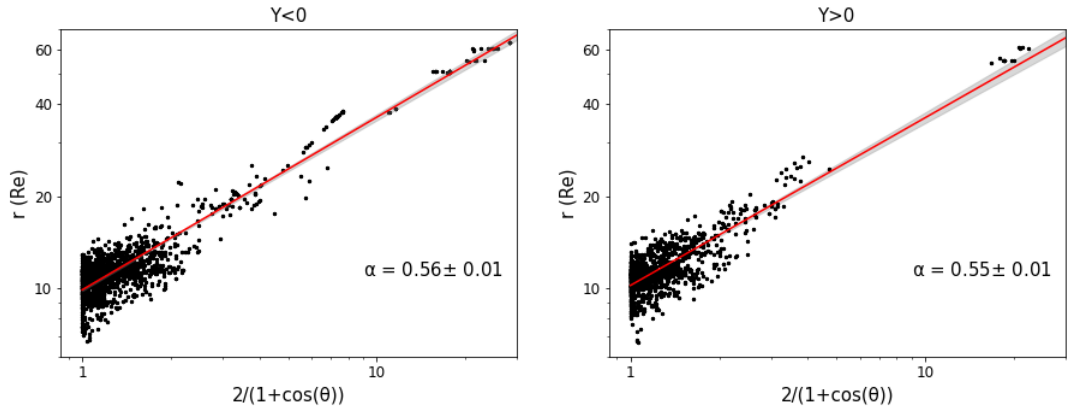

Figure 8. The same figure than 7 but with the crossings in the $Y<0$ (*left*) and in the $Y>0$ (*right*) half-spaces.

5 Magnetopause flaring

Figures 7 and 8 provide evidence of the magnetopause flaring as the power law of an elliptic function consistently with the equation 1. They also show a different flaring α in the $(X-Y)$ and in the $(X-Z)$ directions, indicating the necessity to treat the influence of the various solar wind parameters in the two planes separately.

5.1 Influence of the dynamic pressure

Following our previous results, we now symmetrize the dataset in the Y direction. We focus on the equatorial flaring by selecting the 5443 duskward events for which $|Z|<1\ R_e$ and on the polar flaring by selecting the 4064 northern events for which $|Y|<2\ R_e$. We represent the averaged distribution of the total pressure in these two newly defined $(X-Y)$ and $(X-Z)$ planes in the two panels of Figure 9.

Although the observation is noisier in the left panel, one can see the appearance of clear parallel contours which intercept goes from 15 Re to 7 Re with an increasing pressure. This proves that the main effect of an increasing pressure stands in an earthward translation of the magnetopause along the X axis and thus, that the flaring coefficient of the magnetopause is independent from the upstream solar wind pressure. This finding is consistent with Lin et al. (2010) who found no particular pressure dependency and with the results of Liu et al.

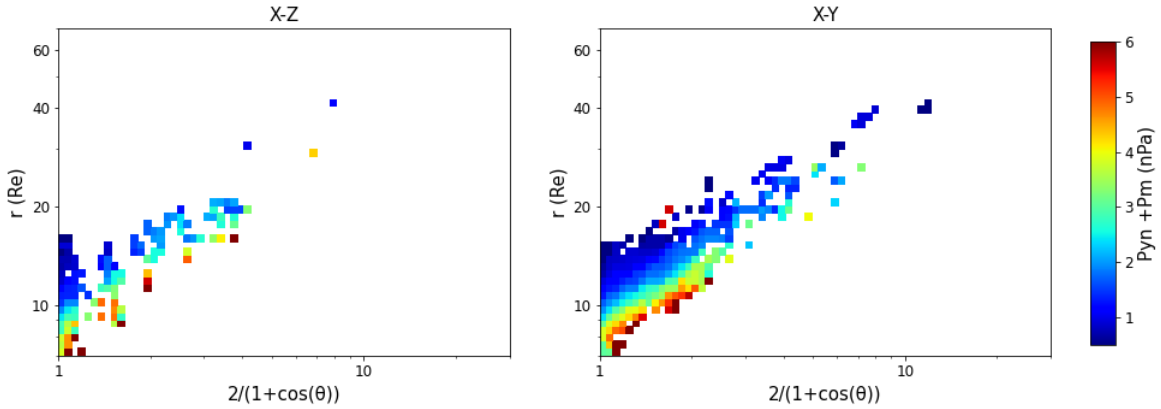

Figure 9. Averaged spatial distribution of the solar wind total pressure ($P_{dyn} + P_m$) associated to the crossings in the $(X - Z)$ (*left*) and in the $(X - Y)$ (*right*) planes.

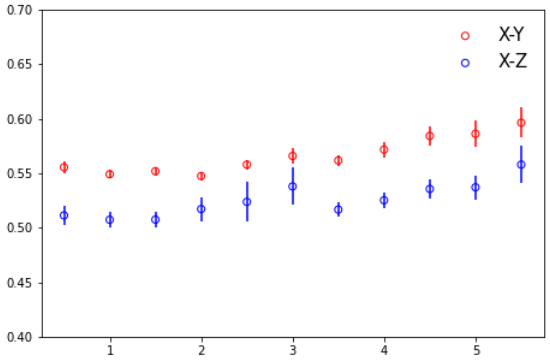

Figure 10. Evolution of the fitted flaring coefficient α as a function of the total pressure for the out of cusps crossings in the $(X - Y)$ (*blue)* and in the $(X - Z)$ (*red*) planes. The error bars represent the 1-sigma confidence intervals of the different fits.

(2015) and Shue et al. (1997) who found a flaring coefficient that had very little variations with the pressure.

Another method we have to evidence this independence consists in separating the data of each plane into sliding pressure bins between 0.5 and 6 nPa and estimating the flaring coefficient α by fitting the radial position of the crossings to the equation 1 with r_0 being defined by the equation 4. The result of such fits is shown in the two planes in Figure 10 and seeing very little variations of α in the two planes confirms the independence.

5.2 Influence of the dipole tilt angle

The dipole tilt angle is expected to only influence the $(X - Z)$ flaring of the magnetopause ((Boardsen et al., 2000; Lin et al., 2010) and references therein). Thus, we investigate the influence of the dipole tilt angle on the flaring by considering the $(X - Z)$ crossings previously defined only. As for the case of pressure, we separate the crossings into sliding 12.5° tilt angle bins and estimate α for each group of events.

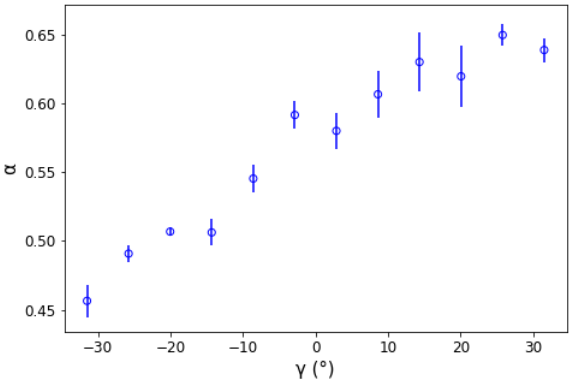

h

Figure 11. Evolution of the fitted flaring coefficient α as a function of the dipole tilt angle γ for the out of cusps crossings in the $(X - Z)$ plane. The error bars represent the 1-sigma confidence intervals of the different fits

The results of the fits are shown in the Figure 11 and shows a clear linear increase of α with an increasing γ. This indicates a northern hemisphere magnetopause that has an increased flaring during summer.

This finding is consistent with the dependencies evidenced by Boardsen et al. (2000) and Lin et al. (2010) and very close from the hyperbolic tangent dependency chosen by Liu et al. (2015). Having a symmetrized dataset, the observed flaring for the southern hemisphere will naturally also be a linear function of γ with the same intercept but an opposite slope.

5.3 Influence of the IMF clock angle

The influence of the IMF orientation on the magnetopause shape was first noticed by Aubry et al. (1970) who noticed, using Ogo 5 measurements, an earthward motion of the boundary when the IMF was southward. The phenomena was later-on frequently found in numerous statistical studies of the magnetopause location and shape (Sibeck et al., 1991; Petrinec & Russell, 1996) and considered in the most recent analytical models through the dependence on the IMF B_z component for both the subsolar stand-off distance and the level of flaring (Shue et al., 1997; Lin et al., 2010; Liu et al., 2015; Wang et al., 2013).

The aforementioned models all suggested the cross-section of the magnetopause in the YZ plane would be an ellipse which major axis points in the cGSM Z direction when the IMF points due south.

Such behaviour might be explained by the erosion mechanism resulting from magnetic reconnection and usually described by the so-called *onion peel model* Sibeck et al. (1991). When the IMF points south, the so-believed equatorial X-line leads to a tailward convection of the reconnected flux. This may increase the XZ flaring in the process, although on average should be somewhat balanced by tail reconnection in a steady Dungey cycle. This increase would stop as the IMF becomes northward, a condition for which lobe reconnection will lead to dayside convection, possibly decreasing the XZ flaring down to a point where the major axis of the YZ magnetopause cross-section points along Y.

It is also worth noting that the influence of the IMF orientation might depend on the value of the Alfvén Mach Number. Using MHD simulations, Lavraud and Borovsky (2008) suggested that, at low Mach numbers, resulting in lower magnetosheath plasma β, the magnetic force contracts the magnetopause so that its YZ elliptic cross-section now has

a major axis along Z for both due south and due northward IMF while eastward (resp. westward) IMF rotates the major axis anti-clockwise (resp.clockwise). This twisting of the magnetopause with the clock angle as also been reported by (Liu et al., 2015). It however introduces an asymmetry with respect to the XZ plane which we have not found on average and thus ignored in the current study. We will thus only focus on XZ and XY flarings.

We now investigate the influence of the IMF clock angle Ω. We consider the events in the $(X-Y)$ (resp. $(X-Z)$) plane and separate them into 30° (resp. 60° wide clock angle bins between -180 ° and 180 ° and estimate α for each group of events. The obtained values are shown in the Figure 12.

For southward IMF orientations (green shaded intervals), the $(X-Z)$ flaring, represented by the blue dots, is higher than the equatorial flaring represented with the red dots. The major axis of the magnetopause YZ cross-section is then oriented along the cGSM Z axis. For northward orientations (yellow-shaded intervals), the $(X-Z)$ flaring decreases and now becomes lower than the equatorial one, which increases a bit but overall varies less. This evolution is consistent with the suggestions of the other existing empirical magnetopause models (Shue et al., 1997; Lin et al., 2010; Liu et al., 2015; Wang et al., 2013) and could thus possibly be explained by the erosion mechanism triggered by magnetic reconnection. The current study limits the investigation to the $(X-Z)$ and $X-Y$ planes for statistical reasons, further investigations should focus on assessing whether the magnetopause is actually twisted as suggested by both Liu et al. (2015) and Lavraud and Borovsky (2008). Additionally, our results suggest different magnetopause cross-section for due southward and northward IMF orientations, which is different from the suggestions made by Lavraud and Borovsky (2008). This might be due to the fact our results are obtained with no distinction between the low and the high Alfven Mach number and it would thus be interesting, in a further study, to investigate if the result we evidenced still hold for low Alfven Mach number values.

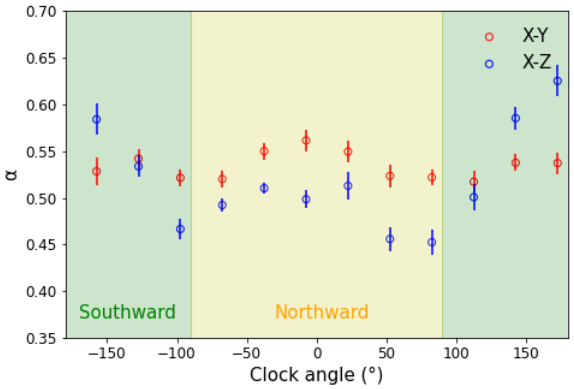

Figure 12. Evolution of the fitted flaring coefficient α as a function of the IMF clock angle for the out of cusps crossings in the $(X-Y)$ *(blue)* and in the $(X-Z)$ *(red)* planes. The green intervals indicate the intervals where the IMF is southward and the yellow interval is the interval of northward IMF. The error bars represent the confidence intervals of the different fits.

The flaring coefficients evolves with the IMF clock angle. This suggests a dependence on the IMF B_y component. To assess this, we consider the 890 events in the $(X-Z)$ plane for which 1 nT $< B_z <$ 3 nT and the 772 events in the $(X-Z)$ plane for which -3 nT $< B_z < -1$ nT . In the two cases, we separate the events into 1 nT wide $|B_y|$ bins and estimate α for each group of events. The obtained values are shown in the Figure 13.

For a negative B_z (green dots), increasing the absolute value of B_y results in a decreasing flaring coefficient. By contrast, the $(X - Z)$ flaring stays roughly constant or mildly increases as $|B_y|$ increases for a positive B_z. These evolutions are consistent with the evolution of α with the clock angle, as shown in the Figure 12.

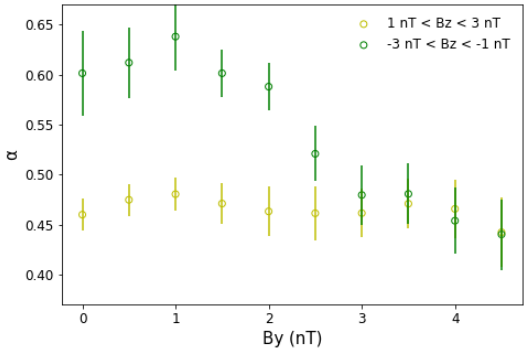

Figure 13. Evolution of the fitted flaring coefficient α as a function of the IMF $|B_y|$ component for the out of cusps crossings in the $(X - Z)$ plane for which 1 nT $< B_z <$ 3 nT (yellow) and for which -3 nT $< B_z < -1$ nT (green). The error bars represent the confidence intervals of the different fits.

5.4 Primary expressions of the flaring coefficient

Following what was done with r_0, the influences of both the Earth dipole tilt angle and the IMF clock angle can be translated into primary empirical analytical expressions describing the magnetopause flaring in the $(X - Y)$ and in the $(X - Z)$ planes.

Applying the Levenberg-Marquardt fitting method to the 5443 events of the $(X - Y)$ plane, we obtain:

$$\alpha = 0.56 + 0.015\cos(\Omega) \tag{5}$$

In a similar manner, the same method applied to the 2047 events of the $(X - Z)$ plane leads us to:

$$\alpha = 0.5 + 0.016\gamma - 0.05\cos(\Omega) \tag{6}$$

Naturally, these two expressions can be generalized to all azimuthal angle ϕ through the fit of the general expression of the magnetopause surface function (1) to the entire symmetrized dataset. This issue is addressed in the second companion paper of our study (Nguyen et al., 2020b).

6 Conclusion

In this paper, we conducted a statistical study on the magnetopause location and shape, based on the combination of the automatically detected multi-mission crossings of Nguyen et al. (2020a) and older crossings accessible online. In particular, we have investigated how the stand-off distance and the equatorial and meridional flaring depend on the solar wind pressure and IMF clock angle.

Our findings can be summarized as follows:

1. The stand-off distance depends on the solar wind (dynamic and magnetic) pressure as a power law which exponent is found very close to the theoretical $-1/6$, consistently with previous studies such as Šafránková et al. (2002); Shue et al. (1997); Lin et al. (2010); Liu et al. (2015).
2. The stand-off distance decreases with as the IMF becomes more strongly southward, the model describes by Shue et al. (1997) matches this variation better than other models.
3. The radial position of the magnetopause is well described by the inverse trigonometric function proposed by Shue et al. (1997) up to lunar distances.
4. We found no particular influence of the IMF cone angle component on the stand-off distance. The sunward motion suggested by Grygorov et al. (2017) as B_x gets stronger is thus not found. It however appeared to be of order of model errors in that region. Further investigation is needed to clarify the possible dependency of the magnetopause flaring on the cone angle.
5. The clock angle is found to influence the flaring of the magnetopause, not only via the B_z component, but also via the B_y one. The equatorial $(X-Y)$ flaring is roughly constant or weakly increases for northward IMF. The $(X-Z)$ meridional flaring however strongly increase as the IMF turns south. For these southward IMF, the $(Y-Z)$ cross-section of the magnetopause is well described by an ellipse which major axis points along Z. For northward cases however, the decrease of the meridional $(X-Z)$ flaring and the weak increase of the equatorial $(X-Y)$ flaring make the ellipse more elongated in the Y direction. Although further detailed investigations are needed to understand the physical effects at the root of these observations, they are consistent with a picture where reconnection carries flux into the lobe in southward conditions, leading to periods of larger $(X-Z)$ flaring. For statistical reasons, we limited our study to the $(X-Y)$ and $(X-Z)$ planes and symmetrized our dataset, thereby excluding the question of the continuous magnetopause twisting with the IMF as suggestion by Liu et al. (2015) and Lavraud and Borovsky (2008). Future investigations, using more data, should address this delicate point.

These different findings pave the way to the construction of a new asymmetric magnetopause shape and location model. This issue will be adressed in Nguyen et al. (2020b) that comes as a companion paper of this study.

Finally, this study was performed on the magnetopause crossings outside of the cusp region and thus gives elements to three of the issues mentioned in the introduction: the influences of the IMF cone and clock angle and the behavior of the magnetopause in the far nightside. It would be interesting to give a specific insight on the near-cusp crossings of our dataset to figure out the actual existence or absence of indentation of the magnetopause in this region. This last issue will be addressed in the third companion paper of our study Nguyen et al. (2020c).

Appendix A Spherical coordinates

We define the spherical equivalent (R, θ, ϕ) of the cartesian GSM coordinates (X, Y, Z) according to the Figure A1. $R = \sqrt{X^2 + Y^2 + Z^2}$ is the radial distance from the center of the Earth, θ is the zenith angle between the direction of R and the X axis and the azimuth ϕ is the angle between the projection of R in the $Y-Z$ plane and the positive direction of the Z axis:

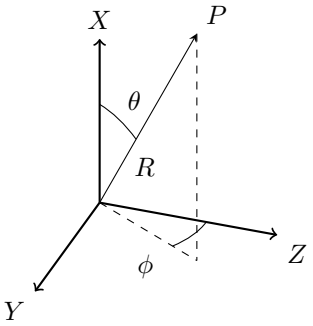

Figure A1. Representation of the spherical equivalent of the cartesian GSM coordinates used in this paper.

$$X = R\cos(\theta) \tag{A1}$$
$$Y = R\sin(\theta)\sin(\phi) \tag{A2}$$
$$Z = R\sin(\theta)\cos(\phi) \tag{A3}$$

Acknowledgments

Enter acknowledgments, including your data availability statement, here.

References

Aubry, M. P., Russell, C. T., & Kivelson, M. G. (1970). Inward motion of the magnetopause before a substorm. *Journal of Geophysical Research (1896-1977)*, *75*(34), 7018-7031. Retrieved from `https://agupubs.onlinelibrary.wiley.com/doi/abs/10.1029/JA075i034p07018` doi: 10.1029/JA075i034p07018

Boardsen, S. A., Eastman, T. E., Sotirelis, T., & Green, J. L. (2000). An empirical model of the high-latitude magnetopause. *Journal of Geophysical Research: Space Physics*, *105*(A10), 23193-23219. Retrieved from `https://agupubs.onlinelibrary.wiley.com/doi/abs/10.1029/1998JA000143` doi: 10.1029/1998JA000143

Cahill, L. J., & Amazeen, P. G. (1963). The boundary of the geomagnetic field. *Journal of Geophysical Research (1896-1977)*, *68*(7), 1835-1843. Retrieved from `https://agupubs.onlinelibrary.wiley.com/doi/abs/10.1029/JZ068i007p01835` doi: 10.1029/JZ068i007p01835

Dmitriev, A. V., & Suvorova, A. V. (1999, November). Artificial neural network model of the dayside magnetopause: physical consequences. *Physics and Chemistry of the Earth C*, *25*, 169-172.

Dušík, Š., Granko, G., Šafránková, J., Němeček, Z., & Jelínek, K. (2010, October). IMF cone angle control of the magnetopause location: Statistical study. *Geophysical Research Letters*, *37*(19), L19103. doi: 10.1029/2010GL044965

Eastman, T. E., Sotirelis, T., & Green, J. L. (2000). An Empirical Model of the High-latitude Magnetopause. *Journal of Geophysical Research*, *105*(1998). doi: doi:10.1029/1998JA000143

Fairfield, D. H. (1971, Jan). Average and unusual locations of the Earth's magnetopause and bow shock. *Journal of Geophysical Research*, *76*(28), 6700. doi: 10.1029/JA076i028p06700

Formisano, V. (1979, Dec). The three-dimensional shape of the bow shock. *Planetary and Space Science*, *2C*, 681-692. doi: 10.1007/BF02558125

Grygorov, K., Šafránková, J., Němeček, Z., Pi, G., Přech, L., & Urbář, J. (2017). Shape of the equatorial magnetopause affected by the radial interplanetary magnetic field. *Planetary and Space Science*, *148*, 28 - 34. Retrieved from `http://www.sciencedirect.com/science/article/pii/S0032063317302131` doi: https://doi.org/10.1016/j.pss.2017.09.011

Hasegawa, H. (2012, August). Structure and Dynamics of the Magnetopause and Its Boundary Layers. *Monographs on Environment, Earth and Planets*, *1*(2), 71-119. doi: 10.5047/meep.2012.00102.0071

Kuznetsov, S. N., & Suvorova, A. V. (1998, January). Solar wind magnetic field and pressure during magnetopause crossings at geosynchronous orbit. *Advances in Space Research*, *22*(1), 63-66. doi: 10.1016/S0273-1177(97)01101-0

Lavraud, B., & Borovsky, J. E. (2008). Altered solar wind-magnetosphere interaction at low mach numbers: Coronal mass ejections. *Journal of Geophysical Research: Space Physics*, *113*(A9). Retrieved from `https://agupubs.onlinelibrary.wiley.com/doi/abs/10.1029/2008JA013192` doi: https://doi.org/10.1029/2008JA013192

Lavraud, B., Fedorov, A., Budnik, E., Grigoriev, A., Cargill, P., Dunlop, M., ... Balogh, A. (2004, August). Cluster survey of the high-altitude cusp properties: a three-year statistical study. *Annales Geophysicae*, *22*(8), 3009-3019. doi: 10.5194/angeo-22-3009-2004

Lavraud, B., Larroque, E., Budnik, E., Génot, V., Borovsky, J. E., Dunlop, M. W., ... Rème, H. (2013). Asymmetry of magnetosheath flows and magnetopause shape during low alfvén mach number solar wind. *Journal of Geophysical Research: Space Physics*, *118*(3), 1089-1100. Retrieved from `https://agupubs.onlinelibrary.wiley.com/doi/abs/10.1002/jgra.50145` doi: https://doi.org/10.1002/jgra.50145

Lavraud, B., Phan, T., Dunlop, M., Taylor, M., Cargill, P., Bosqued, J., ... Fazakerley, A. (2004, August). The exterior cusp and its boundary with the magnetosheath: Cluster multi-event analysis. *Annales Geophysicae*, *22*(8), 3039-3054. doi: 10.5194/angeo-22-3039-2004

Lin, R. L., Zhang, X. X., Liu, S. Q., Wang, Y. L., & Gong, J. C. (2010, Apr). A three-dimensional asymmetric magnetopause model. *Journal of Geophysical Research (Space Physics)*, *115*(A4), A04207. doi: 10.1029/2009JA014235

Liu, Z., Lu, J. Y., Wang, C., Kabin, K., Zhao, J. S., Wang, M., ... Zhao, M. X. (2015). Journal of Geophysical Research : Space Physics A three-dimensional high Mach number asymmetric magnetopause model from global MHD simulation. *Journal of Geophysical Research*, 5645–5666. doi: 10.1002/2014JA020961.Received

Liu, Z. Q., Lu, J. Y., Kabin, K., Yang, Y. F., Zhao, M. X., & Cao, X. (2012, July). Dipole tilt control of the magnetopause for southward IMF from global magnetohydrodynamic simulations. *Journal of Geophysical Research (Space Physics)*, *117*(A7), A07207. doi: 10.1029/2011JA017441

Lu, J. Y., Liu, Z. Q., Kabin, K., Zhao, M. X., Liu, D. D., Zhou, Q., & Xiao, Y. (2011, September). Three dimensional shape of the magnetopause: Global MHD results. *Journal of Geophysical Research (Space Physics)*, *116*(A9), A09237. doi: 10.1029/2010JA016418

Newville, M., Stensitzki, T., Allen, D. B., & Ingargiola, A. (2014, September). *LMFIT: Non-Linear Least-Square Minimization and Curve-Fitting for Python.* Zenodo. Retrieved from `https://doi.org/10.5281/zenodo.11813` doi: 10.5281/zenodo.11813

Nguyen, G., Aunai, N., Michotte de Welle, B., Jeandet, A., Lavraud, B., & Fontaine, D. (2020a). *Massive multi-missions statistical study and analytical modeling of the Earth magnetopause: 1 - A gradient boosting based automatic detection of near-Earth regions.* (Submitted)

Nguyen, G., Aunai, N., Michotte de Welle, B., Jeandet, A., Lavraud, B., & Fontaine, D. (2020b). *Massive multi-missions statistical study and analytical modeling of the Earth magnetopause: 3 - An asymmetric magnetopause analytical model.* (Submitted)

Nguyen, G., Aunai, N., Michotte de Welle, B., Jeandet, A., Lavraud, B., & Fontaine, D. (2020c). *Massive multi-missions statistical study and analytical modeling of the Earth magnetopause: 4- On the near-cusp magnetopause indentation.* (Submitted)

Němeček, Z., Šafránková, J., & Šimůnek, J. (2020). An examination of the magnetopause position and shape based upon new observations. In *Dayside magnetosphere interactions* (p. 135-151). American Geophysical Union (AGU). Retrieved from https://agupubs.onlinelibrary.wiley.com/doi/abs/10.1002/9781119509592.ch8 doi: 10.1002/9781119509592.ch8

Petrinec, S. M., & Russell, C. T. (1993, December). An empirical model of the size and shape of the near-Earth magnetotail. *Geophysical Research Letters*, *20*(23), 2695-2698. doi: 10.1029/93GL02847

Petrinec, S. M., & Russell, C. T. (1996). Near-earth magnetotail shape and size as determined from the magnetopause flaring angle. *Journal of Geophysical Research: Space Physics*, *101*(A1), 137-152. Retrieved from https://agupubs.onlinelibrary.wiley.com/doi/abs/10.1029/95JA02834 doi: 10.1029/95JA02834

Roelof, E. C., & Sibeck, D. G. (1993, December). Magnetopause shape as a bivariate function of interplanetary magnetic field B_z and solar wind dynamic pressure. *Journal of Geophysical Research*, *98*(A12), 21421-21450. doi: 10.1029/93JA02362

Shue, J. H., Chao, J. K., Fu, H. C., Russell, C. T., Song, P., Khurana, K. K., & Singer, H. J. (1997, May). A new functional form to study the solar wind control of the magnetopause size and shape. *Journal of Geophysical Research*, *102*(A5), 9497-9512. doi: 10.1029/97JA00196

Sibeck, D. G., Lopez, R. E., & Roelof, E. C. (1991, Apr). Solar wind control of the magnetopause shape, location, and motion. *Journal of Geophysical Research*, *96*(A4), 5489-5495. doi: 10.1029/90JA02464

Sotirelis, T., & Meng, C.-I. (1999, April). Magnetopause from pressure balance. *Journal of Geophysical Research*, *104*(A4), 6889-6898. doi: 10.1029/1998JA900119

Tsyganenko, N. A. (1998, October). Modeling of twisted/warped magnetospheric configurations using the general deformation method. *Journal of Geophysical Research*, *103*(A10), 23551-23564. doi: 10.1029/98JA02292

Šafránková, J., Němeček, Z., Dušík, v., Přech, L., Sibeck, D. G., & Borodkova, N. N. (2002). The magnetopause shape and location: a comparison of the interball and geotail observations with models. *Annales Geophysicae*, *20*(3), 301–309. Retrieved from https://www.ann-geophys.net/20/301/2002/ doi: 10.5194/angeo-20-301-2002

Wang, Y., Sibeck, D. G., Merka, J., Boardsen, S. A., Karimabadi, H., Sipes, T. B., ... Lin, R. (2013, May). A new three-dimensional magnetopause model with a support vector regression machine and a large database of multiple spacecraft observations. *Journal of Geophysical Research (Space Physics)*, *118*, 2173-2184. doi: 10.1002/jgra.50226

Yang, Y.-H., Chao, J. K., Lin, C.-H., Shue, J.-H., Wang, X.-Y., Song, P., ... Lazarus, A. J. (2002). Comparison of three magnetopause prediction models under extreme solar wind conditions. *Journal of Geophysical Research: Space Physics*, *107*(A1), SMP 3-1-SMP 3-9. Retrieved from https://agupubs.onlinelibrary.wiley.com/doi/abs/10.1029/2001JA000079 doi: 10.1029/2001JA000079

Zhou, X.-W., & Russell, C. T. (1997). The location of the high-latitude polar cusp and the shape of the surrounding magnetopause. *Journal of Geophysical Research: Space Physics*, *102*(A1), 105-110. Retrieved from https://agupubs.onlinelibrary.wiley.com/doi/abs/10.1029/96JA02702 doi: 10.1029/96JA02702

Šafránková, J., Dušík, , & Němeček, Z. (2005). The shape and location of the high-latitude magnetopause. *Advances in Space Research*, *36*(10), 1934 - 1939. Retrieved from http://www.sciencedirect.com/science/article/pii/S0273117705004795 (Solar Wind-Magnetosphere-Ionosphere Dynamics and Radiation Models) doi: https://doi.org/10.1016/j.asr.2004.05.009